






The Milky Way Project: Bridging Intermediate- and High-Mass Star Formation with the MIRION Catalog of Yellowballs

KATHRYN DEVINE ¹, GRACE WOLF-CHASE ², C. R. KERTON ³, NICHOLAS LAROSE ³, MAYA COLEMAN,¹
MAKENZIE STAPLEY,¹ ETHAN BASSINGTHWAITE,¹ BEZAWIT MEKASHA KASSAYE,¹ HRITIK RAWAT,¹ AND
THARINDU JAYASINGHE ⁴

¹*The College of Idaho, 2112 Cleveland Blvd., Caldwell, ID 83605, USA*

²*Planetary Science Institute, 1700 East Fort Lowell, Suite 106, Tucson, AZ 85719 USA*

³*Iowa State University, Department of Physics and Astronomy, 2323 Osborn Dr. Ames, IA 50011, USA*

⁴*Independent Researcher, San Jose, CA, USA*

(Accepted 4 December, 2025)

Submitted to ApJ

ABSTRACT

We describe the construction and use of the Mid-InfraRed Interstellar Objects and Nebulae (MIRION) catalog, which was compiled from 6176 objects identified as “yellowballs” (YBs) by participants in the Milky Way Project. The majority of YBs are compact photodissociation regions generated by intermediate- and high-mass young stellar objects that are embedded in star-forming clumps ranging in mass from $10^{10^6} M_{\odot}$ and luminosity from $10^{10^4} L_{\odot}$. The MIRION catalog increases the number of candidate intermediate-mass star-forming regions (SFRs) by nearly two orders of magnitude, providing an extensive database with which to explore the transition from isolated low-mass to clustered high-mass star formation. The catalog comprises five tables that include mid- and far-infrared photometry; velocities of source-associated molecular clouds; distances to these molecular clouds; physical properties of source-associated star-forming clumps; and source crossmatches with other catalogs. The structure of the catalog enables users to easily sort objects for further study based on distance or environmental properties. Our preliminary analysis extends our earlier findings that indicate a relationship between IR colors and the physical properties and evolutionary stages of SFRs. Photometry will be periodically updated online to incorporate measurements from volunteers participating in a classroom activity known as the People Enabling Research: a Yellowball Survey of the Colors Of Protostellar Environments (PERYSOPE) Project. These updates will continue to refine the IR flux measurements and reduce photometric errors. A follow-up paper will present a detailed analysis of how IR colors can be used to predict the properties of star-forming environments.

1. INTRODUCTION

This paper presents the Mid-InfraRed Interstellar Objects and Nebulae (MIRION) Catalog, which contains infrared fluxes, distances, and catalog crossmatches of objects identified as “yellowballs” (YBs) by participants in the Milky Way Project (MWP) (Simpson et al. 2012). The MWP was a citizen-science project hosted on the Zooniverse.org platform. Most of the 6176 objects in the MIRION catalog of yellowballs are star-forming regions (SFRs), and evidence indicates that many of these are associated with newly-identified Intermediate-Mass SFRs (IMSFRs) that are producing stars of mass less than 8–10 M_{\odot} (Wolf-Chase et al. 2021, hereafter WKD21). Therefore, these data observationally probe environments that can help address the question: what causes the transition from low-mass (isolated) to high-mass (clustered) star formation?

Just as solid-state physicists can learn about the nature of materials by studying phase transitions (Canfield 2020), astrophysicists can learn about the nature of star formation by identifying and studying objects that trace an analogous

Corresponding author: K. Devine

Email: kdevine@collegeofidaho.edu, gwchase@psi.edu, kerton@iastate.edu, nrlarose@iastate.edu

“phase transition” between low- and high-mass star formation. Previous research efforts exploring this transition have been hampered by the low number (~ 50) of identified IMSFRs (e.g., [Arvidsson et al. 2010](#)). The MIRION catalog fills this observational gap by increasing the number of candidate SFRs producing stars with maximum masses of 3–8 M_{\odot} by nearly two orders of magnitude.

MWP participants serendipitously discovered a sample of ~ 900 YBs as part of a project aimed at identifying the infrared bubbles/rings in the Milky Way described by [Simpson et al. \(2012\)](#). YBs are compact objects whose distinct yellow appearance arises from overlapping 8- and 24- μm emission, which were assigned green and red colors, respectively, in the Spitzer images used by the MWP. [Kerton et al. \(2015, hereafter KWA15\)](#) showed that many YBs are young, compact photo-dissociation regions (PDRs), which are likely precursors to H II regions. In this case the 8- μm emission is produced by UV-excited polycyclic aromatic hydrocarbons (PAHs) and the 24- μm emission by warm dust.

KWA15 worked with a YB sample identified by chance. A subsequent iteration of the MWP set YBs as a target ([Jayasinghe et al. 2019](#)), during which volunteers identified over 6000 of these objects from Spitzer surveys covering the inner Galactic plane ($|\ell| \lesssim 65^{\circ}$: [Benjamin et al. 2003](#); [Carey et al. 2009](#); [Churchwell et al. 2009](#)), the Cygnus-X complex ($\sim 24 \text{ deg}^2$ centered on $\ell \sim 79.3$, $b \sim 1^{\circ}$: [Hora et al. 2007](#); [Beer et al. 2010](#)), and a portion of the outer Galaxy ($\ell \sim 102^{\circ} - 109^{\circ}$, $b \sim 0^{\circ} - 3^{\circ}$: [Carey et al. 2008](#)). WKD21 published the locations and user-measured radii of these YBs, as well as the results of a pilot-region study of ~ 500 YBs in a 20 deg^2 region of the Galactic Plane between $\ell = 30^{\circ} - 40^{\circ}$. Details of the construction of the YB database from the raw citizen-science measurements are also presented in WKD21.

WKD21 identified many more YBs with lower luminosity than those studied in KWA15, and they derived physical properties of YB environments using associations with cores/clumps in the Hi-GAL compact source catalog ([Elia et al. 2017](#)). The study demonstrated that YBs identify a mix of young IMSFRs and massive SFRs. This makes these sources particularly interesting, as they highlight the locations of compact (sub-parsec) SFRs that have a wide range of luminosity ($10^{10.4} L_{\odot}$) and mass ($10^{10.6} M_{\odot}$). The YB database expands the number of candidate IMSFRs and identifies many environments thought to be precursors to optically revealed Herbig Ae/Be nebulae.

KWA15 and WKD21 found that many YBs have infrared colors that are distinct from both H II regions and evolved objects such as PNe. Furthermore, the results from WKD21 provided intriguing evidence suggesting that color trends are associated with the physical properties and evolutionary stages of YB environments, but their small sample was insufficient to draw conclusions that would fully describe this relationship.

The new MIRION catalog includes infrared photometry values, photometric errors, and reliability flags at 8, 12, 24, and 70 μm for the full set of 6176 YBs identified by MWP volunteers. Together with catalog crossmatches, the new distances we present enable the determination of physical properties (e.g., mass and luminosity) for 3945 catalog objects. A subsequent paper will present the results of analyzing color trends by the physical properties and evolutionary stages of their environments. With this paper, we also rename these sources from YBs to “MIRION catalog sources,” to more appropriately reflect the fact that MIRION sources are heterogeneous and do not represent a single class of object.

The remainder of this paper is organized as follows: Section 2 summarizes the structure and content of the entire MIRION catalog. Details of the infrared photometry are described in Section 3. Section 4 explains the methods used to determine the distance to the MIRION sources, and Section 5 describes the procedure used for catalog crossmatching. We provide preliminary analysis of the catalog’s contents in Section 6 and present a summary and conclusions in Section 7.

2. CATALOG CONTENT AND STRUCTURE

The MIRION catalog’s data are organized into five tables presenting photometry measurements (Table 1), velocities (Table 2), distances (Table 3), physical properties for Herschel-matched objects (Table 4), and catalog crossmatches (Table 5). The catalog pairs each object with a unique source identification number that is included in every table to facilitate queries involving multiple properties or associations. The descriptive Tables 1–5 presented in this paper provide information about the form and content of each part corresponding table in the MIRION catalog. In the following paragraphs we provide additional information on the content to facilitate use of the catalog.

Columns 2–8 of Table 1 contain the basic positional and size information of the MIRION sources. Details of the construction of the MIRION catalog from MWP volunteer inputs, including information about the user-measured radius and hit rate parameters, is provided in Section 2 of WKD21. While collecting photometric measurements for

this paper we observed that MIRION sources 3035–3101 had a small systematic positional offset (0.35 to 0.1 arcmin between $\ell \sim 101.23^\circ - 103.65^\circ$). We speculate this offset was introduced during the aggregation process of volunteer observations. Coordinates for these sources have been adjusted to match the actual source position seen in the Spitzer images. The photometric data and flags in Table 1 are discussed in Section 3.

Section 3 describes the challenges facing infrared photometry in the Galactic plane, and the need for multiple measurements of each source to reduce error and uncertainty in the photometric flux measurements presented in the MIRION catalog. A participatory-science experience designed for astronomy students (Section 3.2) allows users to contribute additional photometry measurements to this work. The ongoing nature of this project means that the MIRION catalog’s photometric measurements are continually being refined, and periodic updates will be published to the online catalog. The latest version of the entire catalog is available as an online-only resource ⁵.

Velocity and distance information for MIRION sources is given in column 2 of Table 2 and column 3 of Table 3, respectively. The remaining columns of Table 2 provide more detailed information about the type of molecular-line spectrum used (column 4), the various source surveys (columns 5 – 11), and comparative values from other studies (columns 13 and 14). Section 4.2 describes the full procedure used to obtain these data. Similarly, columns 4–7 of Table 3 provide comparative distance information from other studies, and columns 8–16 provide input and output values associated with the distance finding techniques detailed fully in Section 4.3.

Table 4 lists physical properties of Herschel-detected clumps (Elia et al. 2017, 2021) associated with MIRION sources. A detailed description of each quantity along with our error propagation technique is provided in WKD21. Table 5 provides information about crossmatches between MIRION sources and other catalogs of objects related to star formation. The catalog crossmatching technique is described in Section 5 and the properties of MIRION objects with Herschel clump associations are explored in Section 6.

3. SOURCE PHOTOMETRY AND FLAGGING

To conduct photometry and determine infrared colors of the MIRION sources, we follow a procedure similar to the one employed by WKD21. WKD21 used Spitzer Space Telescope images for 8 and 24 μm flux measurements and WISE catalog images for measurement at 12 μm . 70 μm measurements were obtained from the Hi-GAL compact source catalog by Elia et al. (2017). We extended the WKD21 pilot study by collecting photometric data for the full MWP catalog of 6176 YBs, and conducted new photometric measurements of the sources at 8, 12, 24, and 70 μm . Image data used for photometry were obtained at 8 μm from the Spitzer GLIMPSE survey (Benjamin et al. 2003; Churchwell et al. 2009; GLIMPSE team 2020), 12 μm from the WISE catalog (Wright et al. 2010; NASA/IPAC Infrared Science Archive 2020), 24 μm from the Spitzer MIPS GAL survey (Carey et al. 2009; MIPS GAL team 2020), and 70 μm from the PACS survey (PHPDP team 2020). The Cygnus-X legacy survey (Hora et al. 2007; Cygnus-X Team 2020) provided images for 466 catalog sources at all four wavelengths, and the SMOG legacy survey (Carey et al. 2008) provided images for 262 sources at all four wavelengths (S. Carey, private communication 2022).

Complex backgrounds in the Galactic plane at MIR wavelengths make automated photometry methods ineffective. WKD21 developed a program to interactively conduct photometric measurements in their pilot region. After this pilot study, the program was modified to additionally include 70 μm measurements. Figure 1 outlines the photometry process for a representative source. The program loads an image centered on the target object, and the user interactively selects at least three points to generate a polygon that contains the source and distinguishes it from the local background. The program masks the region within these selected points and uses a multiquadratic radial basis function to create a background estimate over the masked area. Finally, the program subtracts this background-only image from the original, resulting in an image of the isolated source, and the flux density is calculated from this “source-only” image. All of the image files (8, 12, 24, and 70 μm) were re-gridded to match the pixel size of the 8 μm image to help users be more consistent with the mask region selection process and make the photometry more consistent across wavelengths.

To reduce the uncertainty introduced by variations in the user-based selection of points, we collected a minimum of five measurements at each wavelength for each source. The number of measurements conducted at each wavelength is listed in Table 1. Additional measurements will be obtained to further reduce uncertainty in the full catalog through a participatory science outreach effort described in Section 3.2.

⁵ <https://github.com/astrodevine/MIRION>

Table 1. MIRION Catalog – Photometry

Number	Units	Label	Explanation
1	—	ID	Source identification number
2	deg	GLON	Galactic longitude
3	deg	GLAT	Galactic latitude
4	deg	MWPR	MWP radius
5	deg	e_GLON	Uncertainty in Galactic longitude
6	deg	e_GLAT	Uncertainty in Galactic latitude
7	deg	e_MWPR	Uncertainty in MWP radius
8	—	HRATE	MWP hit rate
9	Jy	F8	Flux density at 8 μm
10	Jy	e_F8	Uncertainty in flux density at 8 μm ^a
11	Jy	F12	Flux density at 12 μm
12	Jy	e_F12	Uncertainty in flux density at 12 μm ^a
13	Jy	F24	Flux density at 24 μm
14	Jy	e_F24	Uncertainty in flux density at 24 μm ^a
15	Jy	F70	Flux density at 70 μm
16	Jy	e_F70	Uncertainty in flux density at 70 μm ^a
17	—	N8	Number of photometric measurements at 8 μm
18	—	N12	Number of photometric measurements at 12 μm
19	—	N24	Number of photometric measurements at 24 μm
20	—	N70	Number of photometric measurements at 70 μm
21	—	f_SAT	Saturation flag ^b
22	—	f_MULTI	Multiple source flag ^c
23	—	f_NOSRC	No clear source flag ^b
24	—	f_PCONF	Poor confidence in photometry ^b
25	—	f_CEXT	Highly circular extended source ^c

^aFractional error: standard deviation/flux density

^bFour-digit integer with each place corresponding a particular band.

^cSingle-digit integer. Set to 1 if flag criteria is met in any band.

NOTE—Table 1 is published in its entirety in the electronic edition of the *Astrophysical Journal*. A descriptive table is shown here for guidance regarding its form and content.

3.1. Flagging

The sources in the MIRION catalog are highly heterogeneous and represent a range of objects. To note complications in the data and interesting morphological features, flags are listed in the catalog in Table 1. These flags were assigned by visual inspection of source-only, background-subtracted images, which were generated using a method similar to that described in the previous section. The flagging code retrieves the coordinates of the masks generated by all of the users who measured the photometry on a given source, and then creates an average mask for the source region by including masked pixels that were selected by at least half of the users who had inspected the source. We then used this average mask to generate source-only images to be examined for flagging. Each source within the catalog was inspected visually and flags were applied. Columns 21–25 of Table 1 show these flags, with 0 indicating no flag and 1 indicating a flag.

Table 2. MIRION Catalog – Velocities

Number	Units	Label	Explanation
1	—	ID	Source identification number
2	km s ^{−1}	VLSR	Adopted V_{LSR}
3	km s ^{−1}	e_VLSR	Uncertainty in adopted V_{LSR}
4	—	SType	Type of spectrum ^a
5	km s ^{−1}	VLSR_G	V_{LSR} from GRS
6	km s ^{−1}	VLSR_S	V_{LSR} from SEDIGISM
7	km s ^{−1}	VLSR_F	V_{LSR} from FCRAO OGS
8	km s ^{−1}	VLSR_T	V_{LSR} from ThrUMMS
9	km s ^{−1}	VLSR_DHT	V_{LSR} from DHT surveys
10	km s ^{−1}	VLSR_DGT	V_{LSR} from dense gas tracer (DGT) surveys
11	—	DGT	DGT survey used for column 10
12	km s ^{−1}	VLSR_C	V_{LSR} from Elia et al. (2021)
13	km s ^{−1}	VLSR_M	V_{LSR} from Mège et al. (2021)
14	km s ^{−1}	e_VLSR_M	Uncertainty in V_{LSR} from Mège et al. (2021)

^aSP = single peak, MP: n = multiple (n) peaks, LSNR = low SNR, and OUT = outside of molecular line survey coverage.

NOTE—Table 2 is published in its entirety in the electronic edition of the *Astrophysical Journal*. A descriptive table is shown here for guidance regarding its form and content.

Images that are saturated and cannot be used for photometry are denoted by flag “f_SAT.” Some sources revealed multiple point sources, particularly at 8 μm , denoted by flag “f_MULTI.” Multiple sources often appear in the 8 μm image due to the higher resolution at this wavelength, which reveals filaments or other complex features that appear to be simple, circular sources at longer wavelengths. Some sources that appeared “yellow” in the MWP images used to generate the original YB database do not have obvious emission at all 8, 12, 24, and 70 μm wavelengths, denoted with the “f_NOSRC” flag. Sources for which the photometry methods failed to yield reliable results (e.g. sources appearing against a highly complex background) are flagged with a “f_PCONF” flag. Finally, a small number of sources presented interesting, very round structures that are likely planetary nebulae or compact bubbles. These sources are flagged with a “f_CEXT” flag. Figure 2 shows example sources to which flags were applied. While most of the flags designate potential issues with the photometry, f_MULTI and f_CEXT sources are flagged as sources of interest for follow-up studies. For example, some “f_MULTI” sources may represent star-forming regions just at the evolutionary stage where their stellar content is being revealed at shorter MIR wavelengths. There are 1938 sources in the MIRION catalog sources are flagged with f_MULTI, and 18 are flagged with f_CEXT.

While the f_MULTI and f_CEXT flags are not wavelength dependent, the f_SAT, f_NOSRC, and f_PCONF flags may be required at some wavelengths and not others. Thus, these three flags are all represented as four-digit strings for flags at 8, 12, 24, and 70 μm respectively. For example, a flag f_NOSRC=0011 indicates no obvious source at 24 and 70 μm , while a flag f_NOSRC=1000 indicates no obvious source at 8 μm . A f_PCONF=0100 flag would indicate poor confidence in the 12 μm photometry for that source, and a f_SAT=0010 flag would indicate that the 24 μm image is saturated for that source.

3.2. Participatory Science through PERYScope

To collect more photometric measurements and thereby reduce the uncertainty in our photometry measurements, we have developed the People Enabling Research: A Yellowball Survey of the Colors of Protostellar Environments (PERYScope) Project. The PERYScope Project is aimed primarily towards introductory-level astronomy students, but can be adapted to any interested group of volunteers. PERYScope includes an activity guide, instructional videos,

Table 3. MIRION Catalog – Distances

Number	Units	Label	Explanation
1	—	ID	Source identification number
2	kpc	DIST	Adopted distance
3	kpc	e_DIST	Uncertainty in adopted distance
4	kpc	DIST_C	Distance from Elia et al. (2021)
5	kpc	DIST_M	Distance from Mège et al. (2021)
6	kpc	e_DIST_M	Uncertainty in distance from Mège et al. (2021)
7	—	STAT_M	Status flag from Mège et al. (2021)
8	—	PFAR	P_{far} parameter for Reid et al. (2019) distance finder (RDF)
9	kpc	DIST_R1	Most probable RDF distance
10	kpc	e_DIST_R1	Uncertainty in most probable RDF distance
11	—	PINT_R1	Integrated probability for most probable RDF distance
12	—	ARM_R1	Name of associated spiral arm for most probable RDF distance ^a
13	kpc	DIST_R2	Second-most probable RDF distance
14	kpc	e_DIST_R2	Uncertainty in second-most probable RDF distance
15	—	PINT_R2	Integrated probability for second-most probable RDF distance
16	—	ARM_R2	Name of associated spiral arm for second-most probable RDF distance ^a

^aSee [Reid et al. \(2019\)](#) for spiral arm model details.

NOTE—Table 3 is published in its entirety in the electronic edition of the *Astrophysical Journal*. A descriptive table is shown here for guidance regarding its form and content.

and a beginner-friendly version of the photometry code developed using Google Colab that allows participants to learn how astronomers collect and use photometry data in their research.

PERYSCOPE participants are expected to collect and analyze data on a set of around 40 YBs over one or two class or lab periods. Participants are encouraged to submit their data to our database and are given the option to be acknowledged in publications where their measurements are used. PERYSCOPE user measurements will be used to refine the photometric measurements, and will be periodically incorporated into the online version of the MIRION catalog. User-generated data will be compared to the photometry published with this paper for quality control prior to inclusion in the online catalog. Photometric measurement consistency and overlap of the user-selected source region with the average selected region will be examined as inclusion criteria.

4. DISTANCES

4.1. Data

To obtain velocity and distance estimates for MIRION sources, we used the CO molecule and its isotopes (e.g. ^{12}CO , ^{13}CO), as these sources are expected to form within molecular clouds. The MIRION sources are categorized into four regions based on their spatial coverage: the first Galactic quadrant (Q1), the fourth Galactic quadrant (Q4), SMOG and Cygnus-X. The primary survey used for Q1 is the Boston University-Five College Radio Astronomy Observatory Galactic Ring Survey (hereafter GRS, [Jackson et al. \(2006\)](#)). The GRS covers a majority of MIRION sources within Q1, with complete coverage from $l=18^\circ$ - 55.7° , and partial coverage down to $l=14^\circ$. It makes use of the ^{13}CO ($J=1\rightarrow 0$) rotational transition, has a spectral resolution of 0.2 km s^{-1} , and has a velocity coverage from -5 to 135 km s^{-1} for $l\leq 40^\circ$, -5 to 85 km s^{-1} for $l>40^\circ$.

On its own, the GRS does not have complete coverage for Q1; consequently, we supplemented GRS with data from the Structure, Excitation and Dynamics of the Inner Galactic Interstellar Medium survey (SEDIGISM, ([Schuller et al. 2021](#))). SEDIGISM observed ^{13}CO and $\text{C}^{18}\text{O}(J=2\rightarrow 1)$ from $l=-60^\circ$ to 18° , with a spectral resolution of 0.25 km s^{-1} . While this survey contains most of the MIRION sources within Q4, we used the ThrUMMS survey ([Barnes et al.](#)

Table 4. MIRION Catalog – Herschel-Matched Sources

Number	Units	Label	Explanation
1	—	ID	Source identification number
2	pc	DIAM	Diameter
3	pc	e_DIAM	Uncertainty in diameter
4	M_{\odot}	MASS	Mass
5	M_{\odot}	e_MASS	Uncertainty in mass
6	L_{\odot}	BLUM	Bolometric luminosity
7	L_{\odot}	e_BLUM	Uncertainty in bolometric luminosity
8	L_{\odot}/M_{\odot}	LMRAT	Bolometric luminosity/mass ratio
9	L_{\odot}/M_{\odot}	e_LMRAT	Uncertainty in bolometric luminosity/mass ratio
10	K	TEMP	Temperature from graybody fit
11	K	e_TEMP	Uncertainty in temperature
12	—	LRAT	Luminosity ratio
13	—	e_LRAT	Uncertainty in luminosity ratio
14	K	TBOL	Bolometric temperature
15	K	e_TBOL	Uncertainty in bolometric temperature
16	g cm^{-2}	SIGMA	Surface density
17	g cm^{-2}	e_SIGMA	Uncertainty in surface density

NOTE—Columns 2, 4, 6, and 8 contain distance-dependent quantities that have been rescaled using the adopted distances in Table 3. Columns 10, 12, 14, and 16 contain distance-independent quantities.

NOTE—Table 4 is published in its entirety in the electronic edition of the *Astrophysical Journal*. A descriptive table is shown here for guidance regarding its form and content.

Table 5. MIRION Catalog – Catalog Cross-matches

Number	Units	Label	Explanation
1	—	ID	Source identification number
2	—	HIGAL	Hi-GAL 360 source identifier
3	—	AGAL	ATLASGAL source identifier
4	—	CORN	CORNISH source identifier
5	—	CORN_T	CORNISH source type
6	—	RMS	RMS source identifier
7	—	RMS_T	RMS source type
8	—	WISE	WISE source identifier
9	—	WISE_T	WISE source type

NOTE—Table 5 is published in its entirety in the electronic edition of the *Astrophysical Journal*. A descriptive table is shown here for guidance regarding its form and content.

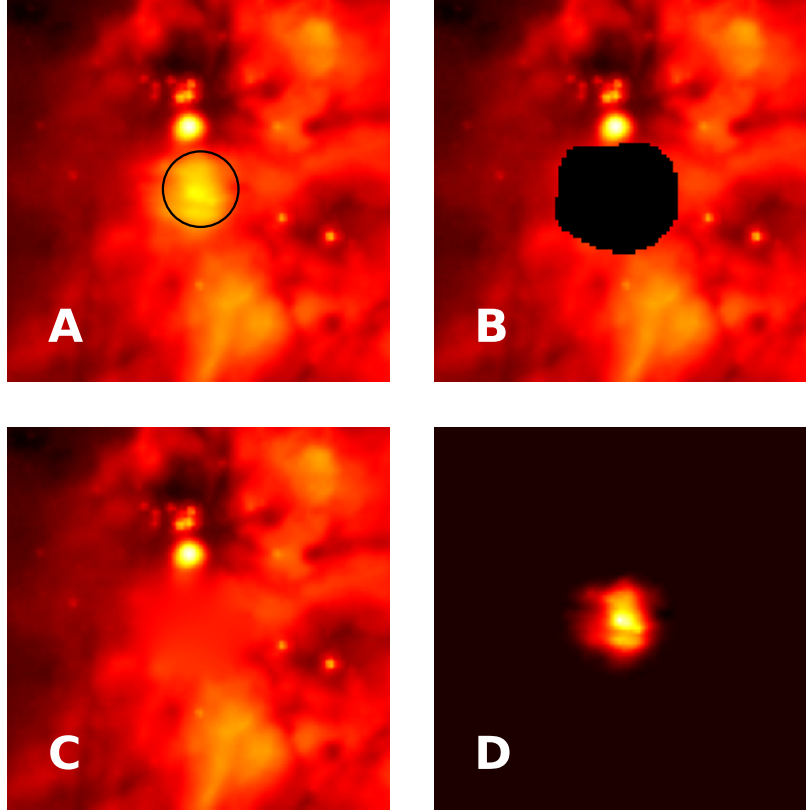


Figure 1. Output images from the Python-based photometry tool used in this work. Upper left panel (A) shows the region containing the source and background emission, where the black circle shows the original MWP average user-selected YB center and radius. Upper right panel (B) shows a user-selected mask covering the source. Bottom left (C) shows the interpolated, background-only image. Bottom t (D) shows the background-removed, source-only image used for photometry.

2015) to extend coverage. ThruMMS observed ^{12}CO , ^{13}CO , and C^{18}O ($J=1\rightarrow 0$) from $l=299^\circ$ to 359° , with a spectral resolution of 0.3 km s^{-1} . For our purposes, ^{13}CO was used for consistency with the other surveys. Both the SMOG and Cygnus-X regions lie outside of the high-resolution CO surveys previously mentioned. For a majority of the SMOG region (from $l > 103.5$), we used ^{12}CO ($J = 1 \rightarrow 0$) data, with $100''44$ spatial resolution and 0.82 km s^{-1} velocity resolution, from the Canadian Galactic Plane Survey (CGPS) (Taylor et al. 2003). These data are re-processed and re-projected versions of data from the Five College Radio Astronomy Observatory (FCRAO) ^{12}CO ($J = 1 \rightarrow 0$) Outer Galaxy Survey (OGS; Heyer et al. (1998)). Details of the incorporation of the OGS into the CGPS are given in Brunt et al. (2003) and Taylor et al. (2003).

For the remaining MIRION objects that were not found within any of the aforementioned surveys, we selected low-resolution CO surveys from the 1.2 meter CO Survey Archive. We utilized eight regions from those available (Dame et al. (1987), Grabelsky et al. (1987), Bronfman et al. (1989), Leung & Thaddeus (1992), Bitran et al. (1997), Dame et al. (2001)) to estimate peak CO velocities, using the higher-resolution surveys before resorting to the low-resolution “Superbeam” survey (Dame et al. 1987). A summary of the CO surveys used, including their observed lines, spatial resolutions, and spectral resolutions, is presented in Table 6.

In an attempt to disambiguate sources with multiple similarly intense peaks (see subsection 4.2), we compared spectra from surveys that trace dense gas or evidence of star formation with CO spectra. MIRION objects are thought to primarily be star-forming regions, and therefore may exhibit signatures of early- or late-stage star formation. Common tracers include maser emission from various molecules, such as OH, CH_3OH , and H_2O . In order to match as many MIRION sources as possible to potential maser sites, we selected large-scale surveys. These surveys include THOR, The HI/OH/Recombination line survey of the Milky Way (Beuther et al. 2019); SPLASH, the Southern Parkes Large-Area Survey in Hydroxyl (Dawson et al. 2022); and HOPS, the H_2O southern Galactic Plane Survey (Walsh et al.

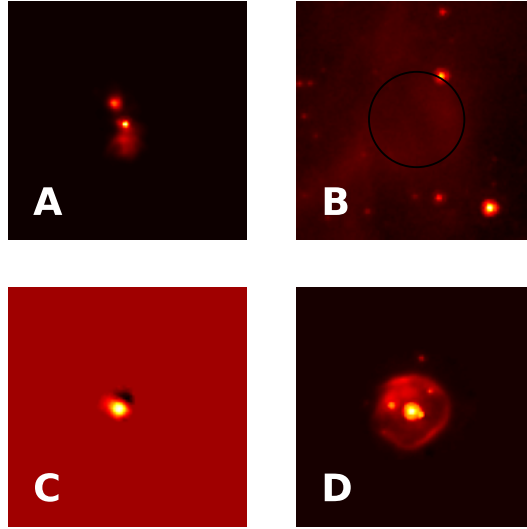


Figure 2. Representative examples of sources to which flags were applied. All images shown are $8\ \mu\text{m}$ background-subtracted, source-only with the exception of (B) which shows the original region since the source-only image which is not meaningful in this case. (A): multiple sources within the masked region. (B): no obvious source at that wavelength. (C): photometry flagged for poor confidence, in which the background subtraction left a negative-valued region near the source, (D): a very round, extended structure.

2008). SPLASH provided supplemental data from OH maser emission at 1612, 1665, 1667 and 1720 MHz, while HOPS provided H_2O maser emission at 22 GHz and NH_3 (1,1) emission, which traces dense gas in star-forming regions.

4.2. Velocities

We retrieved velocity estimates from CO survey spectral-cube cutouts ($0.64''$ in size) at the location of the MIRION sources. The cutout size is based on the average source size being $\sim 24''$ across (WKD21). This ensures enough of the source is selected for a sufficient signal-to-noise ratio (SNR), but is not too large as to contain unrelated emission. Comparison of a sample of MIRION source velocities to those adopted by WKD21 using a $24''$ search region size resulted in an average percent difference of 7.7%. Increasing this to $48''$ resulted in a smaller percent difference of 2.1%. Some of the largest MIRION sources from WKD21 reach projected radii of $\sim 50''$, meaning selecting a cutout region larger than this would result in unrelated emission for a majority of sources. With these considerations in mind, we adopted a $48''$ search region for velocity estimation. It is important to note that while most MIRION sources do not lie within close proximity to one another (with average separation $> 200''$), there are a few instances of multiple sources residing within the same cutout region. In these cases, we assumed that these objects lie within the same parent structure/molecular cloud, and would therefore share similar line-of-sight radial velocities.

Once we obtained a cutout, we adopted the velocity corresponding to a Gaussian fit about the most intense CO peak (I_{max}) for each object, as this often traces the most dense gas (Ellsworth-Bowers et al. 2015). Peaks were identified as exceeding the “noise floor,” defined as $< I > +3\sigma_I$ for 30 channels near the end of the spectrum. To distinguish between secondary peaks and noise associated with a single major peak, peaks were required stand out from nearby minor peaks in excess of $0.2I_{\text{max}}$.

We flagged sources based on the complexity of their spectra as either single-peaked (SP), multi-peaked (MP), low signal-to-noise ratio (LSN), or outside of the CO surveys (OUT). The LSN flag is used to indicate sources with low SNR (< 2). The MP flag indicates spectra with secondary peaks exceeding $0.8I_{\text{max}}$. In this case, we recorded the number of peaks that met this criterion, and flagged the source for further investigation. Although the most intense peak usually corresponds to the most dense gas, it may not trace where star formation is actively occurring. An example of this is shown in Figure 3.

Table 6. Spectral Line Surveys

Survey	Observed Line	Spatial Resolution	Spectral Resolution
Name		(degrees)	(km s ⁻¹)
FCRAO GRS	¹³ CO (J=1→0)	0.013	0.20
SEDIGISM	¹³ CO (J=2→1)	0.008	0.25
ThrUMMS	¹³ CO (J=1→0)	0.018	0.30
FCRAO SMOG	¹² CO (J=1→0)	0.028	0.82
DHT01	¹² CO (J=1→0)	0.500	0.65
DHT02	¹² CO (J=1→0)	0.125	1.30
DHT08	¹² CO (J=1→0)	0.125	0.65
DHT10	¹² CO (J=1→0)	0.125	0.65
DHT17	¹² CO (J=1→0)	0.125	0.65
DHT18	¹² CO (J=1→0)	0.250	0.65
DHT33	¹² CO (J=1→0)	0.125	1.30
DHT36	¹² CO (J=1→0)	0.125	1.30

NOTE—Surveys used in determining velocities of MIRION objects. The low-resolution survey names (DHT#) are as they appear in the 1.2 meter CO Survey Archive.

To discern whether the CO emission from a MIRION source corresponds to I_{\max} or a secondary peak, we used spectra from various transitions that trace star formation. We used a SNR of 1.75 for defining peaks in dense gas tracers (DGTs). We identified potential DGT matches using the criterion that the FWHM of the original CO peak (or one of the secondary peaks) overlapped the FWHM of the DGT peak. We then inspected these sources to identify true overlaps.

Because the GRS and SEDIGISM surveys overlap in the range $l=0.0\text{--}18.0^\circ$, final velocities need to be determined for sources with velocity estimates from both surveys. In the case of a velocity ambiguity, we adopted the GRS velocity over the SEDIGISM, since GRS has superior spectral resolution. In the case of ambiguity with a SEDIGISM velocity outside of the GRS velocity range (i.e. < -5 km s⁻¹), we compared spectral flags (in order of preference, “SP”, “MP”, then “LSN”). In the case where their spectral flags match, we compared their integrated distance probabilities from Reid (see subsection 4.3). If no CO velocity was found using the available surveys, but the MIRION source spatially matched within 24'' of a Hi-GAL compact source with a known distance (Mège et al. 2021) (hereafter M2021), we adopted the corresponding velocity.

Velocity estimates for all 6176 MIRION sources were obtained using the above methods. Of the primary surveys used, 1830 (29.5%) were determined from the GRS, 2612 (42.3%) from SEDIGISM, 240 (3.9%) from FCRAO SMOG, 597 (9.7%) from ThrUMMS, and 570 (9.2%) from low-resolution CO surveys. The remaining 327 (5.3%) of sources have velocities taken directly from M2021, due to lack of survey coverage or because they met the non-kinematic M2021 criteria. In terms of their spectral flags, 4085 (66.1%) are SP, 849 (13.8%) are LSN, 416 (6.7%) are OUT, and 826 (13.4%) are MP. Of the sources that are MP, 651 contained a single additional peak (MP:1), 127 contained two (MP:2), and 48 contained more than two additional peaks. It is important to note that most of the sources with more than two additional peaks arise from SEDIGISM spectra which approach LSN. Of the MP and LSN sources, 107 (2%) have DGT velocities that differ from the original CO estimates.

4.3. Distance Results

With position and velocity information available for each MIRION source, distances can be estimated using a Galactic rotation model. In our case, we used the Parallax-Based Distance Calculator V2 from Reid et al. (2019). This distance calculator takes as inputs the MIRION source (l,b) coordinates, the LSR velocity and the P_{far} parameter, which is

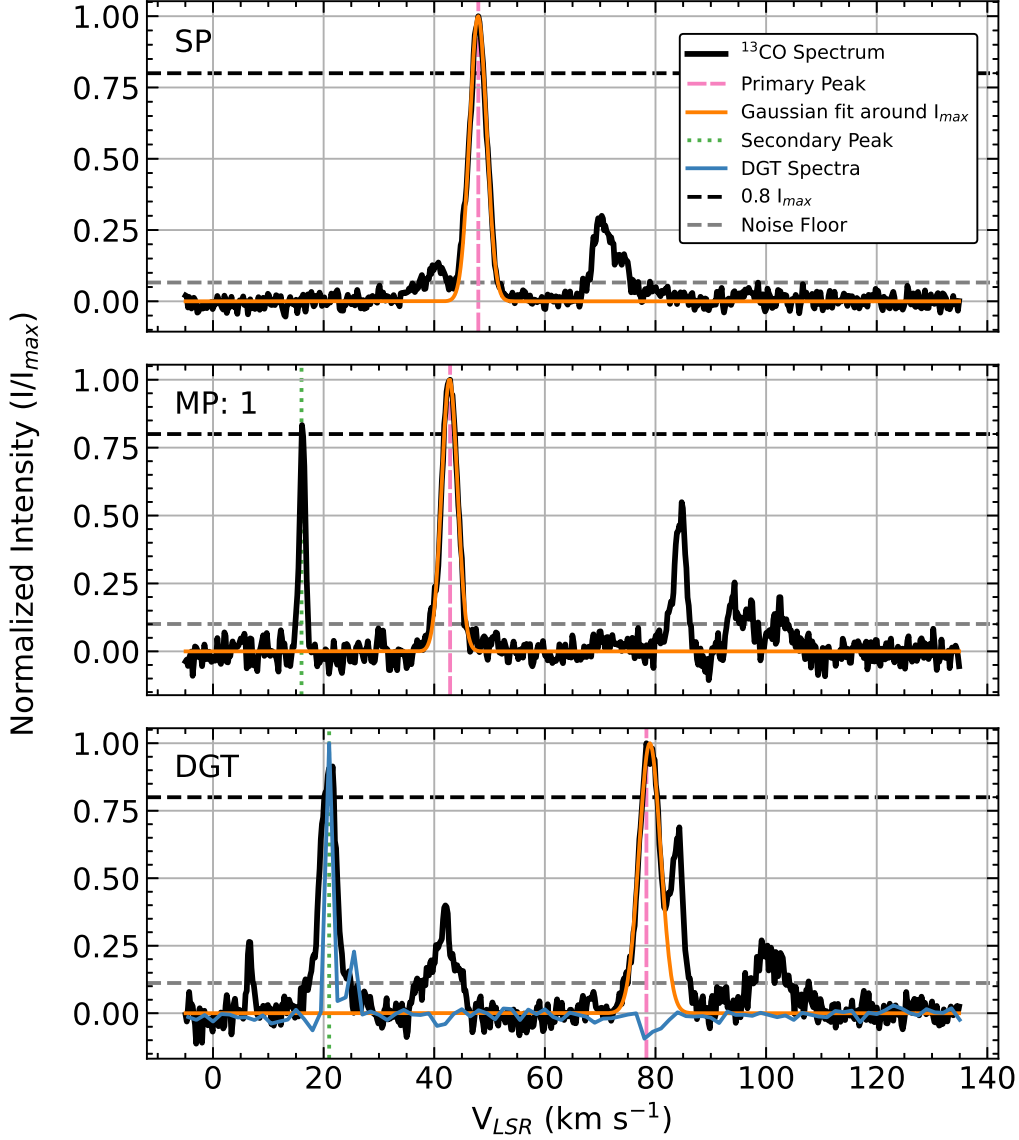


Figure 3. Example MIRION sources showing the different flags used for spectral classification. The top panel shows a SP source, where only one CO peak exceeds $0.8I_{max}$. The middle panel shows a case where a secondary peak exceeds $0.8I_{max}$, marking it as a MP: 1 source. Lastly, the bottom panel shows a source associated with a dense gas tracer (DGT). In this case, the secondary peak coincides with a 1662 MHz OH maser from THOR, and is preferentially adopted over the CO peak with the most intense emission.

the probability that the object lies at the far kinematic distance. The Reid et al. (2019) distance calculator provides a probability-based resolution of the near-far distance ambiguity resulting from using velocity information to estimate distance in the inner galaxy.

To assign P_{far} to the MIRION objects, we obtained Hi-GAL distance results from M2021. M2021 used a variety of distance determination methods to disambiguate Hi-GAL compact sources. Using their results, we compared near (d_{near}), far (d_{far}), and adopted distances (d) for spatially-matched MIRION sources (priority order 3-9 in table 2 from M2021). If, for instance, $d_{near} = d$, we set the P_{far} value to 0.0. A status of MDIST indicates the source distance was determined using maser parallax, while a status of SDIST_GROUP means the stellar distance was determined from grouping using optical H II regions. These methods are non-kinematic and subject to less ambiguity; therefore, we adopted their distances directly. For sources with NO_KDA (no solution at a given velocity and therefore far distance adopted), KDA_NO (no velocity available), TGT_POINT (tangent point distance, or the distance adopted at the

Table 7. Acronyms

Acronym	Description
SP	Single peaked CO spectrum
MP	Multi-peaked CO spectrum
LSN	Low signal-to-noise ratio
OUT	Velocity adopted from Mège et al. (2021)
MDIST*	Maser Distance
SDIST_GROUP*	Stellar distance from grouping
KDA_NO*	No velocity
NO_KDA*	No solution
TGT_POINT*	Tangent point distance (forbidden velocity)
NO_AMB*	No kinematic ambiguity

NOTE—Acronyms presented in this paper. Those with an asterisk are from [Mège et al. \(2021\)](#) table 2.

highest allowed velocity for the model at a given (l,b) when the CO velocity exceeded that value), or those lacking a status outside of the M2021 catalog, we used a constant $P_{\text{far}}=0.5$.

With this information, the Reid calculator outputs the estimated distance, error, total integrated probability of the source being at that distance, and in which spiral arm the source is located. Following the same method as with the velocity determination, if no velocity (and therefore no distance) was found from the CO surveys, but the MIRION source matched a Hi-GAL compact source with a known distance (M2021), we adopted that distance. We determined distance estimates for $\sim 94\%$ of MIRION sources.

4.4. Comparison with Previous Studies

We selected a set of MIRION sources that were also M2021 matches to compare our results with previous studies. Only sources with independent distance estimates were included, totaling 2666 objects. M2021 compared their radial velocity measurements for 5976 sources with those from ATLASGAL ([Urquhart et al. 2018](#)), and found that 89.4% and 91.8% of their sources had velocity differences smaller than 5 km s^{-1} and 10 km s^{-1} , respectively. Comparing MIRION velocities to M2021, we found that 80.2% and 83.3% of matched sources had velocity differences smaller than 5 km s^{-1} and 10 km s^{-1} , respectively.

Additionally, M2021 compared their distances to ATLASGAL by selecting sources outside $\pm 12^\circ$ of the Galactic Center (due to highly uncertain distance determination), including only those with a velocity difference less than 5 km s^{-1} , and not flagged as “NO_KDA”. They found a mean distance difference of 0.21 kpc, with 2248 (64%) of their sources having a difference $< 0.7 \text{ kpc}$. When we compare independent MIRION distances with those of M2021 meeting the same criteria, we find a mean distance difference of 0.3 kpc, with 61% of 1973 matched sources having differences less than 0.7 kpc.

5. SOURCE CROSSMATCHING

To identify MIRION source associations in other catalogs, we crossmatched sources to the same catalogs used in WKD21. We retrieved these catalogs using the VizieR catalog access tool ([Ochsenbein et al. 2000](#)). We performed a $24''$ crossmatch with the Hi-GAL compact source catalog II (3979 sources, [Elia et al. 2021](#)), the ATLASGAL dust condensation catalog (1623 sources, [Csengeri et al. 2014a](#)), the ATLASGAL compact source catalog (CSC) (1563 sources, [Contreras et al. 2013](#)), the RMS survey (613 sources, [Lumsden et al. 2013](#)), the WISE survey (2315 total sources, [Anderson et al. 2014](#)), as well as the CORNISH North (192 sources, [Purcell et al. 2013](#)) and South (384 sources, [Irabor et al. 2023](#)) surveys. The results of this are presented in [Table 8](#).

The Hi-GAL and both ATLASGAL surveys identify compact sources (i.e. clumps, cores) at various stages of evolution using far-IR and sub-mm observations. The ATLASGAL GaussClump Source Catalog (GCSC, [Csengeri](#)

et al. (2014b)) used the GaussClump algorithm, which assumes a Gaussian intensity distribution and is sensitive to angular scales corresponding to both nearby cores and distant clumps. The ATLASGAL CSC used Source-Extractor, which is better suited for molecular clump and cloud structures on a larger scale than the GCSC.

The RMS survey searched for young massive stellar objects and used supplemental surveys at other wavelengths to classify different types of objects (e.g. YSOs, H II regions, Planetary Nebulae). The WISE survey used MIR emission and source morphology to identify candidate and known H II regions, distinguishing sources into categories “K” for known H II regions, “C” for candidate H II regions, “G” for group, and “Q” for radio-quiet sources. The CORNISH surveys used 5 GHz radio continuum to identify H II regions.

To ensure that the crossmatches were not spurious in nature, we created 100 simulated distributions of MIRION sources for each survey. We selected random Galactic longitudes from a uniform distribution within the same longitude range as the surveys. We selected latitudes for each source from Gaussian distributions parameterized by the MIRION source extent in Galactic latitude; for the first and fourth Galactic quadrant we used $\mu = -0.06^\circ$, $\sigma = 0.42^\circ$, and for Cygnus X we used $\mu = 0.73^\circ$, $\sigma = 1.28^\circ$. The MIRION sources from the SMOG region are offset from the Galactic mid-plane and do not resemble a Gaussian distribution. In order to better estimate the Galactic latitude distribution, RMS H II regions / YSOs were used as a proxy for MIRION sources, which (over the SMOG region) exhibit a Gaussian distribution with $\mu = 0.61^\circ$ and $\sigma = 1.74^\circ$.

The simulated MIRION sources were crossmatched to each catalog. This resulted in matches with $3.4\% \pm 0.2\%$ (210 ± 13) of the randomly generated MIRION sources for the Hi-GAL catalog (within the Hi-GAL survey region). For all other surveys, less than 1% of the generated MIRION sources matched with the star formation catalogs. These results are consistent with those presented in WKD21, where the Hi-GAL catalog matched with $4.5\% \pm 0.9\%$ of simulated sources. We maintain that catalog crossmatches can reliably be used to associate MIRION sources with tracers of star formation given the low level of spurious association.

The source “hit rate” reported by the MWP in the creation of the original YB catalog (see Table 1) is another metric by which to judge whether MIRION sources are truly associated with sites of star formation. The hit rate for MIRION sources is the ratio of the total number of times a source was identified by MWP users to the total number of times images containing the source were viewed (WKD21). The hit rate for all 6176 MIRION sources shows a wide distribution, with a mean and standard deviation of 0.40 and 0.19 respectively. This is similar to the distribution of the sample WKD21 studied. The matched surveys and their corresponding mean hit rates for MIRION sources are Hi-GAL (0.43), ATLASGAL Condensations (0.43), ATLASGAL compact sources (0.44), RMS (0.42), WISE (0.48), CORNISH N (0.46), and CORNISH S (0.46), all with standard deviation ~ 0.20 . The mean hit rate for the 1457 MIRION sources without any catalog crossmatches is 0.32 with a standard deviation of 0.15. The difference between the mean hit rates of MIRION sources with and without catalog matches is very similar to what WKD21 found. The lower mean hit rate for unmatched MIRION sources may be explained in part by the fact that many of the unmatched sources have low fluxes and would have been missed by these surveys, although some unmatched objects may be ISM features identified by MWP volunteers that are not actually associated with star-forming regions.

6. ANALYSIS

6.1. Physical Properties of Hi-GAL Associated Clumps

The subset of MIRION sources with Hi-GAL CSC associations are particularly interesting as they are the objects that are most likely associated with star-formation activity. As described in Section 2, Table 4 lists these objects along with both distance-independent and rescaled distance-dependent physical properties. Histograms showing the distribution of the physical properties are shown in Figures 4 and 5, and descriptive statistics are listed in the top rows of Table 9. For this sample we removed 34 sources that were missing one or more physical properties, resulting in a sample of 3945 MIRION sources.

Focusing first on distance-dependent quantities, we find that most of these MIRION sources have masses in the range $0 < \log_{10}(M/M_\odot) < 4$, luminosities in the range $1 < \log_{10}(L/L_\odot) < 5$, and diameters falling in the canonical clump range of 0.2 – 3 pc. These results are similar to those found by WKD21 (compare Table 9 with Table 5 in WKD21).

Distance-independent quantities can be related to the evolutionary stage of the clump or to the mass of the stellar population forming within a clump. Large L/M ratio and surface density values are typically associated with massive SFRs (e.g., Elia et al. 2017). The luminosity ratio, T_{bol} and, to a lesser extent, T_{gray} are all evolutionary stage proxies. The increase in luminosity ratio and T_{bol} reflect the expected shift in the clump SED peak to shorter wavelengths at

Table 8. MIRION Source Crossmatch Results

Survey	Subset	Num. Matches	Percent Match (Survey Range)
Hi-GAL CSC-360		3979	65.26%
ATLASGAL Condensations		1623	30.48%
ATLASGAL CSC2014		1563	41.24%
RED MSX		613	11.03%
WISE	Total	2315	37.48%
WISE	K	435	7.04%
WISE	G	113	1.83%
WISE	C	486	7.87%
WISE	Q	1276	20.66%
CORNISH		576	12.08%

NOTE—Results from the 24'' crossmatch of the MIRION sources with catalogs tracing star formation. Column 4 indicates the fraction of MIRION sources that match with a given object out of the total number of MIRION sources that exist within that survey range.

later evolutionary stages, and the increase in T_{gray} reflects the overall ISM temperature increase expected to occur as stars form within a clump. Comparing Table 9 with Table 5 from WKD21 we can observe that the histogram properties are again very similar. Table 10 summarizes some key threshold values for four of these quantities and compares our results with those found by WKD21, and values derived for the full protostellar Herschel clump sample from [Elia et al. \(2017\)](#).

It is interesting to explore how clump physical properties vary based on different subsets selected via the catalog crossmatching described in Section 5. One simple division is to divide the sample into MIRION sources with and without clear signatures of high-mass star formation. A high-mass signature subsample of 897 objects was defined as MIRION sources having WISE types of C, K, or G; RMS types of H II region or H II/YSO; or CORNISH types of UCH II, H II region (including Diffuse and Dark), MYSO, or IR Quiet. Objects with multiple catalog crossmatches had to meet these criteria in all catalogs. For example, a MIRION source with CORNISH H II region and WISE K crossmatches would be included, but a source with CORNISH H II region and WISE Q crossmatches would not. The distribution of physical properties for this subset is shown as the gold histograms in Figures 4 and 5, and descriptive statistics are listed in the middle rows of Table 9. Descriptive statistics for the complementary sample of objects with no high-mass star-formation signatures are shown in the lower rows of Table 9. For this sample we have removed the stellar and planetary nebula crossmatches resulting in a sample of 2887 sources.

As expected, the histograms associated with signatures of high-mass star formation are skewed towards higher masses and luminosities (top row of Figure 4). There is no significant difference in the diameter distributions of the high-mass sample compared to the full sample. All of the histograms of distance-independent quantities are shifted to larger values in the high-mass sample, as expected for sources that are involved in high-mass star formation, more evolved, or both. Interestingly, while the average surface density also shifts to higher values for this sample, the range of these values remains very large. This is likely the result of high-mass SFRs in our sample being at different stages of evolution. For example, MIRION sources with either an UCH II region association or a Diffuse H II association would both be included, but the associated surface densities are likely to be vastly different due to the clearing of material expected at later stages of massive SFR evolution.

The radar plot shown in Figure 6 compares median distance-independent values for five different crossmatch subsets. We see the CORNISH and RMS subsets are essentially identical in this five-parameter space and have median values expected for evolved, high-mass SFRs. The WISE C/G/K subsample shows there is a significant decrease in the median surface density. This most likely reflects the fact that the WISE-based sample includes more evolved H II regions, which will tend to have a lower surface density due to the removal and dispersal of material caused by the combined action of ionization and stellar winds.

The WISE Q and MIRION only subsamples have median properties that clearly differ from the other subsets to a significant extent. It is tempting to simply conclude that this difference reflects the inability of these clumps to form high-mass stars and that WISE Q and MIRION only clumps are mostly all low- and intermediate-mass SFRs. Such a conclusion, however, fails to consider the impact of these objects’ evolutionary stage of their properties.

The effect of clump evolution on observed clump properties is best illustrated using a luminosity-mass (LM) plot. Figure 7 shows LM plots for four different subsets of MIRION sources. All of the sources selected have low fractional mass and luminosity uncertainties (< 0.5).

The upper-row plots show sources with high-mass star-formation signatures from the RMS and WISE-K surveys. The majority of these points lie above the 90th percentile lower-limit for H II region associated clumps defined by [Elia et al. \(2017\)](#). The lower-row plots show sources that do not have high-mass star-formation signatures. As expected for clumps having some star-formation activity, the majority of these sources lie above the 90th percentile upper-limit for pre-stellar clumps defined by [Elia et al. \(2017\)](#). Comparing this figure to Figure 4 in WKD21, we see the full survey populates the $10 - 100 M_{\odot}$ region more fully, with 378 sources ($\sim 25\%$ of the WISE Q and MIRION Only combined sample) falling in this mass range.

In each plot we have overplotted representative evolutionary tracks and isochrones from the [Molinari et al. \(2008\)](#) model for clump evolution. In this model the star-formation process starts in isolated pre-stellar clumps having a particular mass. The clump then evolves almost vertically on the LM plot as a single intermediate- or high-mass star forms within the clump, reducing its mass slightly while raising the luminosity. The star-formation stage then ends with a dispersal stage in which the luminosity of the clump remains roughly constant as the clump mass decreases. In this model, the observed mass of the clump constrains its future evolutionary path. For example, any clump with a mass between $80 - 350 M_{\odot}$ should follow an evolutionary path resulting in a SFR with a (stellar) luminosity between $2 \times 10^3 - 2 \times 10^4 L_{\odot}$ ($\log_{10}(L/L_{\odot}) = 3.3 - 4.3$). This luminosity range is at the dividing line between high-mass (OB) stars and lower-mass later B-type stars, meaning we can use evolutionary tracks in the $80 - 350 M_{\odot}$ range as a dividing line between clumps associated with high-mass and intermediate/low-mass star formation.

The RMS and WISE K samples in Figure 7 are, by definition, high-mass SFRs, and we find that only 24% of the combined sample have a clump mass $< 350 M_{\odot}$. In contrast, 57% of the combined WISE Q and MIRION-only sample have clump masses $< 350 M_{\odot}$. In the context of the [Molinari et al. \(2008\)](#) evolutionary models, these sources are likely IMSFRs. If we remove the fractional error constraint on these samples this percentage increase to 66%.

We note that more recent models of star formation in clumps ([Molinari et al. 2019](#)) also model the formation of multiple stars within a clump, but they do not try to account for the fact that clumps are not observed to be fully isolated from their surrounding environment and that star formation in clumps likely involves the flow and accretion of material at multiple scales as star formation occurs ([Motte et al. 2018](#)). As a result, the vertical, star-formation portion of the evolutionary tracks shown in Figure 7 become tilted to the right, reflecting the fact that clump mass can increase as star formation occurs. Unfortunately, the evolutionary tracks in this picture are more complex and can become degenerate with the evolutionary track for any particular clump becoming highly dependent on the clump’s surrounding environment ([Krumholz & McKee 2020](#), [Larose et al. in preparation](#)). The range of masses and luminosities spanned by the MIRION catalog makes it an ideal dataset for testing various clump evolutionary models.

6.2. Photometry-Based Analysis

As discussed in Section 3, we made at least five measurements of each source’s flux density at 70, 24, 12, and $8 \mu\text{m}$. Multiple measurements control and quantify the uncertainty that results from users’ differing selections of the area delineating the sources. The mean flux density and the fractional errors (standard deviation/flux density) at each wavelength are reported in Table 1. There are 4757, 4545, 4176, and 4669 sources at 70, 24, 12, and $8 \mu\text{m}$, respectively, having fractional uncertainties less than 0.5. As in WKD21, we use a fractional error of 0.5 as the cut-off for sources’ inclusion in the photometry-based analysis.

Figure 8 shows the distribution of the number of sources by $\log_{10}(F_{12}/F_8)$ color, both for the full catalog and for subgroups of sources with crossmatches in other catalogs. Similar histograms were produced in KWA15 and WKD21, but this study increases the number of sources with both F_{12} and F_8 values below the 0.5 fractional error cut-off by nearly an order of magnitude (3116 sources, as opposed to 324 in WKD21). We find a mean $\log_{10}(F_{12}/F_8)$ color (\pm standard deviation) of -0.48 ± 0.19 for the full sample, very close to the mean value of -0.43 ± 0.15 reported by WKD21. The solid lines in Figure 8 represent the mean value for each plot, while the dashed vertical lines represent the mean value of -0.43 from the WKD21 pilot region.

Table 9. Descriptive Statistics for Hi-GAL Matched Sources

	Mass	Luminosity	Diameter	$L_{\text{bol}}/\text{Mass}$	T_{grey}	L_{ratio}	T_{bol}	Surface Density
	$\log_{10} (M_{\odot})$	$\log_{10} (L_{\odot})$	$\log_{10} (\text{pc})$	$\log_{10} (L_{\odot}/M_{\odot})$	(K)	$\log_{10} (L/L_{\text{SMM}})$	(K)	$\log_{10} (\text{g cm}^{-2})$
Median	2.34	3.14	−0.35	0.91	17.6	1.85	46.5	−0.57
Mean	2.26	3.13	−0.38	0.87	18.3	1.78	46.8	−0.56
SD	0.85	0.99	0.35	0.62	4.7	0.54	11.9	0.56
Max.	4.65	6.28	0.51	2.68	40.0	4.04	162.7	1.14
Min.	−2.51	−1.66	−2.37	−1.71	7.6	−1.00	11.8	−2.00
Median	2.78	4.03	−0.31	1.32	21.2	2.13	52.0	−0.19
Mean	2.65	3.95	−0.37	1.30	21.6	2.07	53.5	−0.20
SD	0.79	0.86	0.35	0.49	5.1	0.46	13.7	0.53
Max.	4.58	6.28	0.51	2.67	39.1	3.49	146.4	1.14
Min.	−1.25	0.10	−2.29	−0.68	8.5	−0.52	17.5	−2.00
Median	2.21	2.89	−0.36	0.75	16.6	1.75	44.7	−0.70
Mean	2.13	2.84	−0.38	0.71	17.2	1.67	44.2	−0.69
SD	0.83	0.87	0.35	0.58	4.1	0.52	10.1	0.51
Max.	4.65	5.65	0.42	2.68	40.0	4.04	162.7	1.13
Min.	−2.51	−1.66	−2.37	−1.71	7.6	−1.00	11.8	−2.00

NOTE—Statistics for three different samples are shown. Top: full MIRION–Hi-GAL sample (3945 sources; large (blue) histograms in Figures 4 and 5). Middle: high-mass SFR signature subsample (897 sources; small (orange) histograms in Figures 4 and 5). Bottom: no high-mass SFR signature subsample (2887 sources). See Section 6.1 for details.

Table 10. Distance Independent Thresholds for Hi-GAL Clumps

Threshold	Percentage of Sample Meeting Threshold				Threshold Interpretation
	MIRION ^a	WKD21 ^b	Protostellar ^c		
$\log_{10} (L_{\text{bol}}/M) > 1.35$	22%	24%	10%		Likely high-mass star formation
$\log_{10} (L/L_{\text{SMM}}) \geq 2$	35%	40%	14%		Older/evolved SFR
$T_{\text{bol}} < 40$	20%	15%	50%		Younger/new SFR
$\log_{10} (\Sigma) > 0$	16%	21%	13%		Likely high-mass star formation

^aHi-GAL matched sample from this paper.

^bHi-GAL matched sample from WKD21.

^cHi-GAL protostellar clump sample from [Elia et al. \(2017\)](#)

In their analysis of YB colors, KWA15 and WKD21 explain that a more compact PDR, with a correspondingly denser radiation field, has a lower $\log_{10}(F_{12}/F_8)$ color. The $\log_{10}(F_{12}/F_8)$ ratio serves as a measure of compactness and PAH ionization. The average $\log_{10}(F_{12}/F_8)$ colors for sources with crossmatches in the RMS, WISE C/G/K, and CORNISH catalogs are -0.37 ± 0.24 , -0.42 ± 0.21 , and -0.39 ± 0.21 , respectively. Notably, all of these subgroups have mean $\log_{10}(F_{12}/F_8)$ colors significantly below the average WISE H II region color of -0.09 reported by [Anderson et al. \(2012\)](#), indicating that MIRION sources correlating to H II regions and MYSOs are still more compact than most WISE catalog sources.

Sources with no crossmatches in the WISE, RMS, or CORNISH catalogs (“No Association” in Fig. 8) have a mean value of -0.49 ± 0.18 , and sources crossmatched with the “radio-quiet” WISE Q sources have a mean value

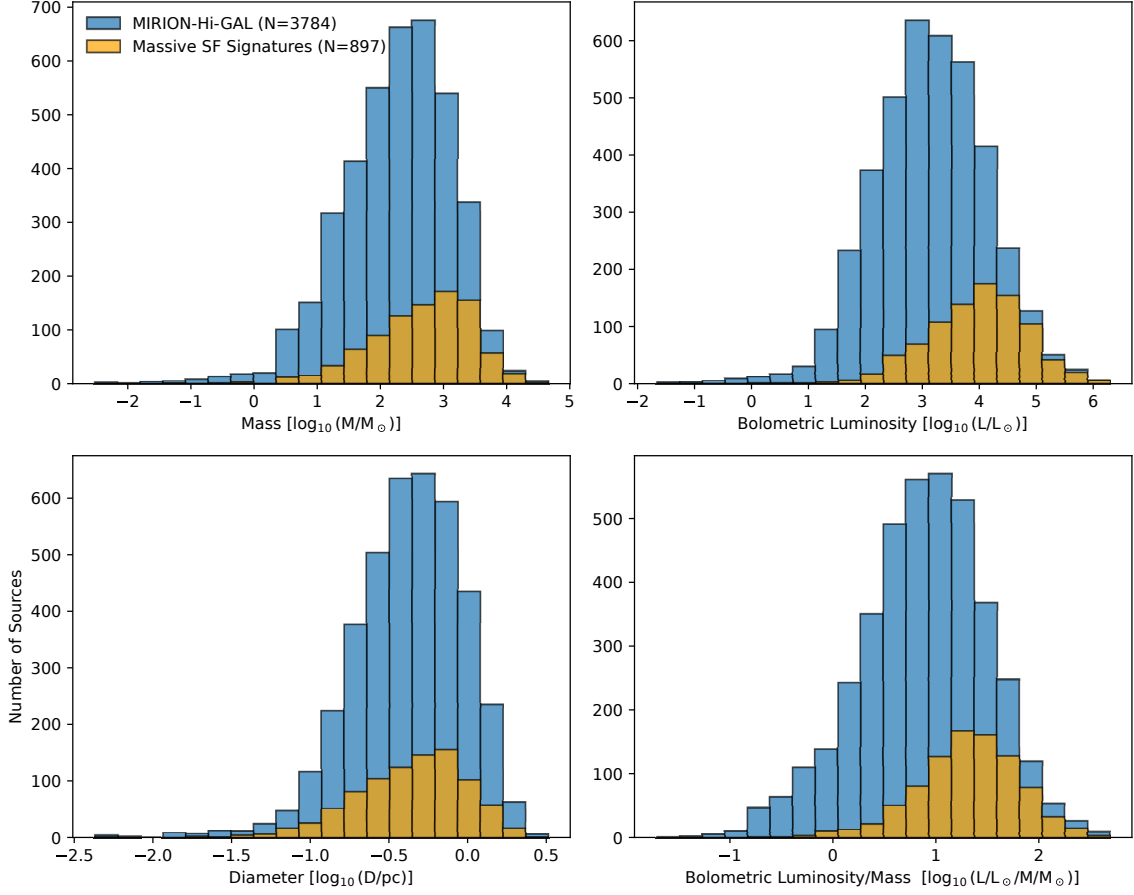


Figure 4. Physical properties of MIRION catalog–Hi-GAL matched sources. Lower-left and upper-row histograms show values from [Elia et al. \(2021\)](#) rescaled using our newly calculated distances. The lower-right panel shows the distance-independent luminosity-mass ratio from [Elia et al. \(2021\)](#). Smaller histograms show the distribution of properties for MIRION objects with clear signatures of massive star formation. See text for full discussion.

of -0.51 ± 0.15 . These values indicate that MIRION sources without H II region and/or MYSO associations are even more compact. These sources represent $\sim 80\%$ of the 3114 sources plotted in Figure 8, further supporting the conclusion from WKD21 that a majority of MIRION sources are highly compact.

IR $\log_{10}(F_{24}/F_8)$ vs. $\log_{10}(F_{70}/F_{24})$ color-color plots are shown in Figure 9. These plots include only sources with no flags for Poor Confidence or No Obvious Source and a fractional error below the 0.5 cut-off, giving a total of 2819 sources. This is an order of magnitude higher than the number of sources analyzed similarly in the WKD21 pilot region (219 sources). In general, the findings using the entire MIRION catalog are consistent with the WKD21 pilot region results. MIRION sources with RMS, CORNISH, or WISE C/G/K counterparts are centered in the average H II color regions from [Anderson et al. \(2012\)](#). This is unsurprising since most of these sources are indeed H II regions. In contrast, MIRION sources with a WISE Q association or no crossmatches in the WISE, RMS, or CORNISH catalogs (“No Association” in Figure 9) are shifted toward lower $\log_{10}(F_{24}/F_8)$. As described in WKD21, higher $\log_{10}(F_{24}/F_8)$ values may serve as an indicator of PAH destruction by hard UV emission, while lower $\log_{10}(F_{24}/F_8)$ values reflect excitation, but not destruction, of PAHs by a softer UV field. MIRION sources with lower $\log_{10}(F_{24}/F_8)$ values are consistent with the expected color trends of intermediate-mass star-forming regions, although some of these sites may eventually produce high-mass stars. Since 60% of the sources included in the Figure 9 analysis are “No Association” sources, and an additional 25% are matched with WISE Q sources, these color-color plots further demonstrate that a majority of MIRION sources are associated with candidate intermediate-mass SFRs.

MIRION sources with lower $\log_{10}(F_{70}/F_{24})$ values in Figure 9 may reflect cooler stellar environments with SEDs that peak at longer wavelengths. The mean value of this ratio does not change significantly across the subgroups plotted in

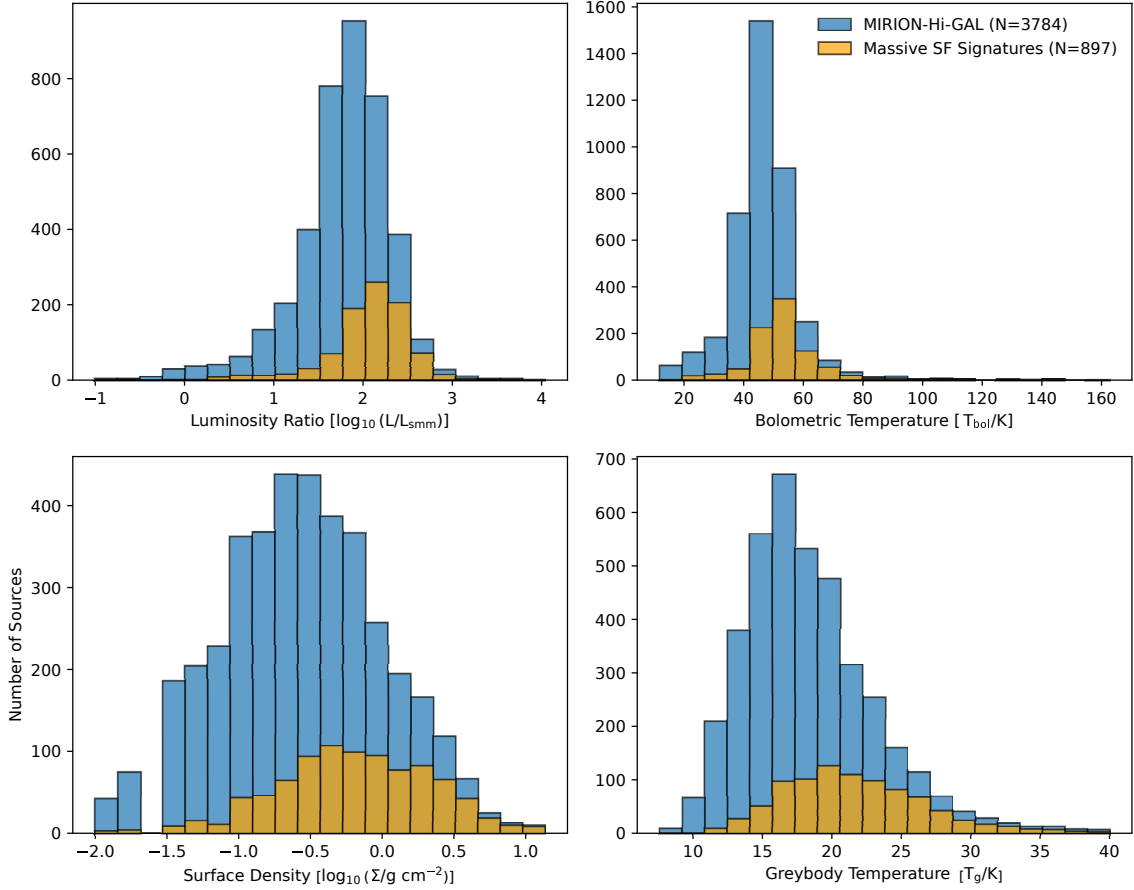


Figure 5. As Figure 4. All quantities plotted are distance-independent.

the figure, indicating the dust temperature in these objects’ environments is similar. Longer wavelength observations spanning the greybody curve of these regions as done by [Elia et al. \(2017\)](#) would better constrain the temperature.

The 0.5 fractional error cut-off used in this analysis was chosen based on preference and to be consistent with the analysis in WKD21. MIRION catalog users can sort and analyze the data based on their own fractional error cut-off choices. To explore the impact of the fractional error cut-off on our conclusions, we examined the distributions shown in Figures 8 and 9 with fractional error cut-offs of 0.3 and 0.7. When the cut-off is adjusted to either of these values, the mean colors shown in Figure 8 change by < 0.02 , while the mean colors shown in Figure 9, change by < 0.05 . Varying the fractional error cut-off within this range does not fundamentally change the results of our analysis.

7. SUMMARY AND CONCLUSIONS

In this work, we presented the MIRION catalog, which contains infrared fluxes, velocities, distances, and catalog crossmatches for all ~ 6000 sources identified as YBs by MWP volunteers, as well as physical properties of sources associated with entries in the Hi-GAL CSC. MIRION catalog entries are heterogeneous and represent a range of objects that share the “yellow” MIR-color signature, which led the MWP volunteers to mark them for inclusion in the catalog. Thus, we have replaced the term “yellowballs (YBs)” with “MIRION sources,” to more accurately reflect the diverse physical nature of these objects.

We have demonstrated that the vast majority of all MIRION sources are compact SFRs. Most are consistent with accreting protoclusters that span a wide range in mass ($0 < \log_{10}(M/M_{\odot}) < 4$) and luminosity ($1 < \log_{10}(L/L_{\odot}) < 5$). Over 50% of MIRION sources may highlight sites of intermediate-mass star formation; however, given uncertainties related to the details of clump evolution we cannot rule out the possibility that some of these sites may eventually produce high-mass stars. This study has included more than an order of magnitude more sources than the WKD21

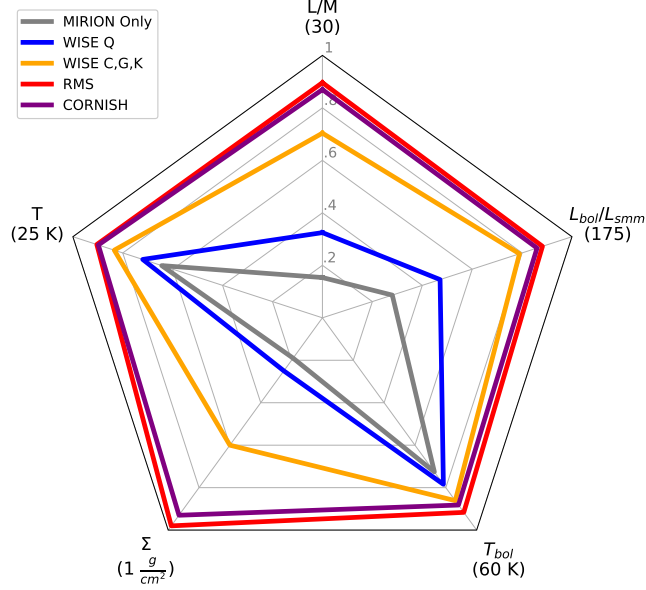


Figure 6. Radar plot representation of five distance-independent quantities for subsets of MIRION sources with Hi-GAL crossmatches. The values shown are medians and are plotted as fractions of the maxima indicated at each radial line. Subsets are based off of source crossmatches with other catalogs, indicated in the legend. L/M : Bolometric luminosity to clump mass ratio; L_{bol}/L_{smm} : Ratio of bolometric luminosity to luminosity calculated in the submillimeter range; T_{bol} : Bolometric temperature; Σ : Clump surface density; T : Dust temperature.

study in its analysis. Of particular significance is the identification of approximately an order of magnitude more sources associated with 10-100 M_{\odot} clumps than were found in the WKD21 study.

Additionally, our large database of infrared flux measurements has enabled us to greatly expand our color-based analysis. The vast majority of MIRION sources have lower $\log_{10}(F_{12}/F_8)$ colors than typical H II regions. Together with the finding that MIRION sources with and without signatures of high-mass star formation (H II regions and high-mass YSOs) have no significant size difference, this suggests that most MIRION sources delineate compact PDRs with high levels of PAH ionization.

Color-color plots indicate a significant $\log_{10}(F_{24}/F_8)$ color difference between sources with and without signatures of high-mass star formation. While MIRION sources with RMS, CORNISH, and WISE C/G/K counterparts occupy the color space associated with H II regions, those with WISE Q and no associations (comprising the majority of all sources) have significantly lower $\log_{10}(F_{24}/F_8)$ colors. This result suggests that these sources identify softer UV environments in which PAH emitters are excited but not destroyed, consistent with expected characteristics of intermediate-mass star formation. Both samples have similar $\log_{10}(F_{70}/F_{24})$ colors, which is consistent with a very slight difference in the median dust temperature between these samples. We conclude that the sources currently lacking indicators of high-mass star formation represent a mix of intermediate-mass star-forming environments and very young regions that may eventually form high-mass stars. We will utilize the MIRION catalog to probe the relationship between IR colors and the evolutionary stage and physical properties of star-forming clumps in a subsequent paper.

ACKNOWLEDGMENTS

The authors wish to thank Sean Carey and Alberto Noriega-Crespo for useful discussions regarding MIPS GAL data. We thank Matt Povich for his work as PI of the MWP, which generated the original yellowball database. We are especially grateful to undergraduate astronomy students who beta-tested the PERYScope materials and contributed their photometric results; these students are listed in Table 11.

Work conducted at The College of Idaho was supported by the Murdock Charitable Trust (Grants NS-2016246, SR-201811723, and SR-202119904). Authors KD, GWC, CK, NL, MC, and EB were supported by NSF Grant No.

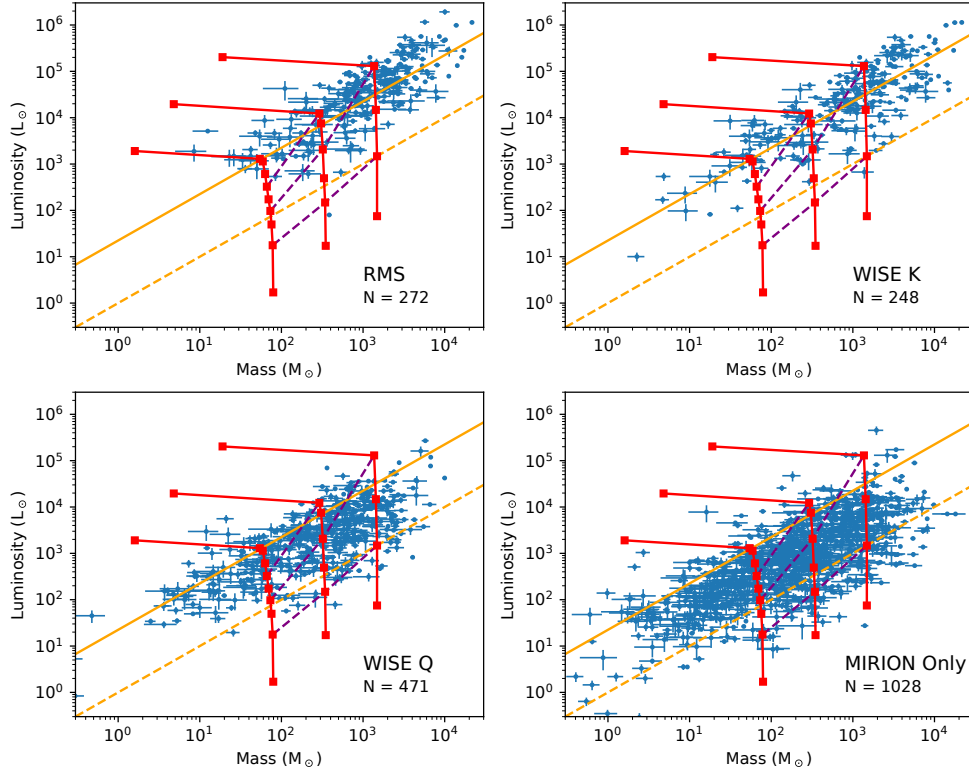


Figure 7. Luminosity-Mass plots for MIRION Catalog sources with Herschel CSC matches. Only sources with fractional error in mass < 0.5 are plotted. Each panel corresponds to objects with a particular catalog association as shown. The yellow diagonal lines correspond to the 90th percentile lower-limit for Herschel-defined H II regions (solid) and the 90th percentile upper-limit for pre-stellar sources (dashed) both defined in [Elia et al. \(2017\)](#). [Molinari et al. \(2008\)](#) clump evolutionary tracks for 80, 350 and 2000 M_{\odot} clumps are shown (red solid lines). Red squares indicate 5×10^4 year intervals on the vertical portions of each track. Three representative isochrones, separated by 10^5 years, are shown as dashed purple lines.

2307806. The PERYSOPE Project development and beta testing was supported by a NASA Citizen Science Seed Funding Grant (Grant No. 20-CSSFP20-001).

This work is based in part on observations made with the Spitzer Space Telescope, which was operated by the Jet Propulsion Laboratory, California Institute of Technology under a contract with NASA. This publication makes use of data products from the Wide-field Infrared Survey Explorer, which is a joint project of the University of California, Los Angeles, and the Jet Propulsion Laboratory/California Institute of Technology, funded by the National Aeronautics and Space Administration. Herschel is an ESA space observatory with science instruments provided by European-led Principal Investigator consortia and with important participation from NASA. This research has made use of the VizieR catalogue access tool, CDS, Strasbourg Astronomical Observatory, France ([Ochsenbein et al. 2000](#)). This research made use of ds9, a tool for data visualization supported by the Chandra X-ray Science Center (CXC) and the High Energy Astrophysics Science Archive Center (HEASARC) with support from the JWST Mission office at the Space Telescope Science Institute for 3D visualization.

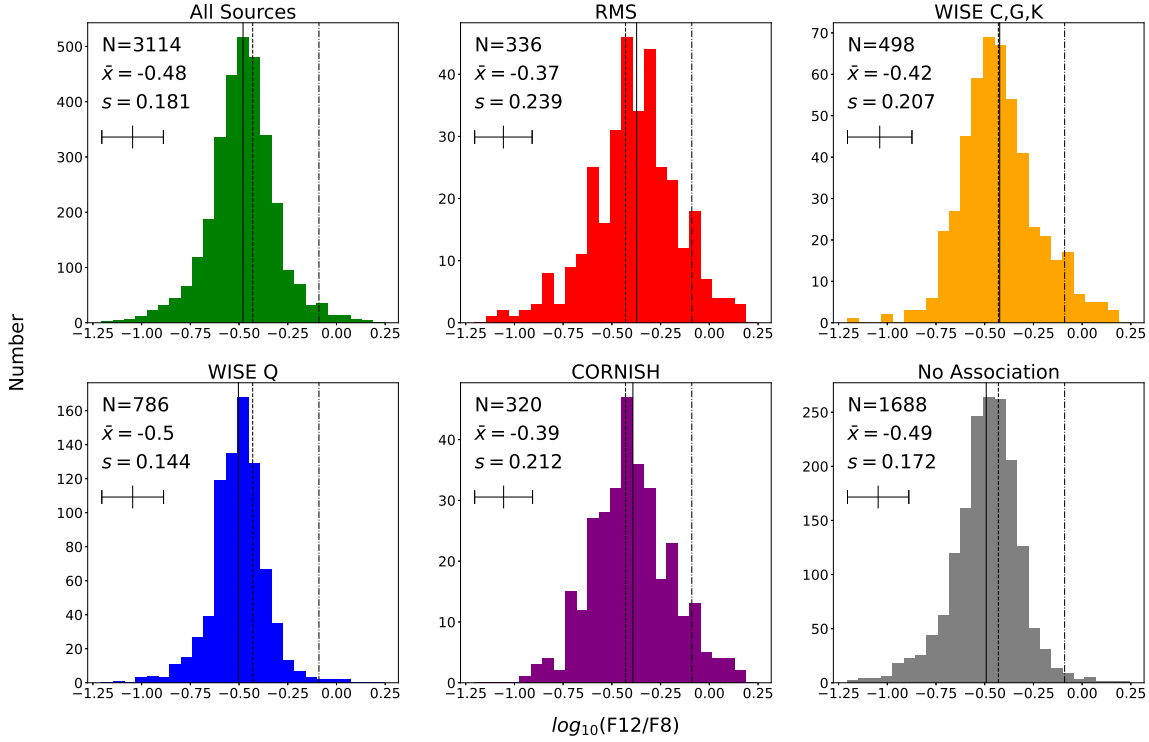


Figure 8. Histograms of the $\log_{10}(F_{12}/F_8)$ color data collected for MIRION catalog sources. Sources with a fractional error of $> .5$ and sources with Poor Confidence or No Obvious Source flags applied at either $12\ \mu\text{m}$ or $8\ \mu\text{m}$ were excluded from the plots. The sources are categorized by crossmatch, with the top left histogram representing all sources, and the bottom right representing sources with no crossmatch in the RMS, WISE, or CORNISH catalogs. The number of sources (N), average color (\bar{x}) and standard deviation (s) for each plot is shown in the top left corner, as well as a barline representing the \pm average uncertainty in the measurements. The solid line is the average color of sources plotted in the histogram, the dashed line is the average color from the [Wolf-Chase et al. \(2021\)](#) pilot region, and the dot-dashed line is the mean H II color from [Anderson et al. \(2012\)](#).

Table 11. PERYSCOPE Participants and Beta-Testers

Santosh Acharya	Tyler Carlson	Bradley Mathew Cushman	Allison Van Dyke
Kat Falk	Brielle Fieuw	Noah Ghiselli	Caden Handran
Jaden Lynn Hernandez	Lex Jones	Brady Joyner	Madeline Khoury
Whitt Miller	Samaje Morgan	Royce Samaniego	Lily Schlake
Asta Shakti Suman Sharma	E.T. Sherwin	Ian Madsen Stowman	Rebecca Amaya Villarreal-Mendoza
Anna Willcuts	JD Willis		

Software: TopCat ([Taylor 2005](#)), Astropy ([Astropy Collaboration et al. 2013](#); [Price-Whelan et al. 2018](#)), Matplotlib ([Hunter 2007](#)), NumPy ([Harris et al. 2020](#)), pandas ([McKinney 2010, 2011](#)), SciPy ([Virtanen et al. 2020](#)).

REFERENCES

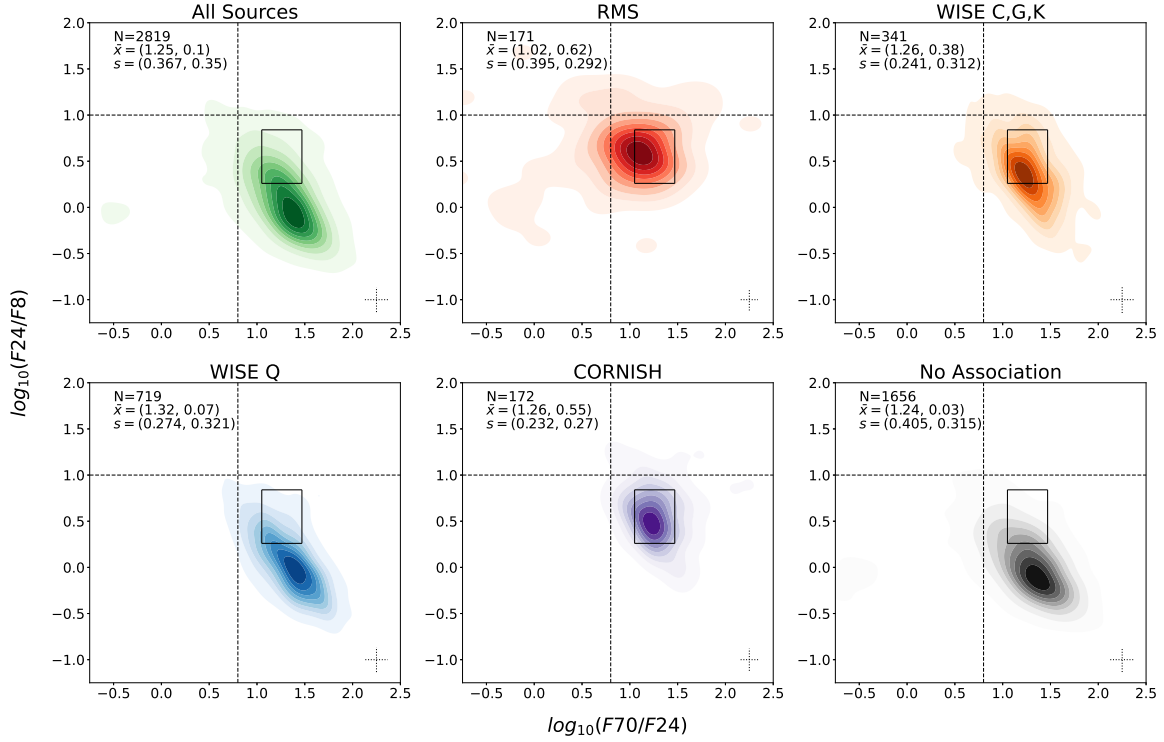


Figure 9. $\log_{10}(F_{24}/F_8)$ vs. $\log_{10}(F_{70}/F_{24})$ color-color kernel density estimate plots created using the photometry data for MIRION catalog sources. Darker colors indicate higher source density in that region. The plots shown exclude sources flagged for Poor Confidence or No Obvious Source, or with a fractional error > 0.5 at $70 \mu\text{m}$, $24 \mu\text{m}$, or $8 \mu\text{m}$. Separate color-color plots were created based on MIRION source crossmatches with other catalogs; the top left plot includes all sources, while the bottom right shows sources with no crossmatch in the RMS, WISE, or CORNISH catalogs. The number of sources plotted (N), average $\log_{10}(F_{70}/F_{24})$ and $\log_{10}(F_{24}/F_8)$ colors (\bar{x}), and standard deviations of the $\log_{10}(F_{70}/F_{24})$ and $\log_{10}(F_{24}/F_8)$ colors (s) are shown in the top left corner for each plot, and the dotted crosshatches in the bottom right corner show the average uncertainties. The dashed lines are the H II -PNe cutoffs from Anderson et al. (2012), and the solid rectangular region indicates the average H II region colors from Anderson et al. (2012).

Anderson, L. D., Bania, T. M., Balser, D. S., et al. 2014, ApJS, 212, 1, doi: [10.1088/0067-0049/212/1/1](https://doi.org/10.1088/0067-0049/212/1/1)

Anderson, L. D., Zavagno, A., Barlow, M. J., García-Lario, P., & Noriega-Crespo, A. 2012, A&A, 537, A1, doi: [10.1051/0004-6361/201117640](https://doi.org/10.1051/0004-6361/201117640)

Arvidsson, K., Kerton, C. R., Alexander, M. J., Kobulnicky, H. A., & Uzpén, B. 2010, AJ, 140, 462, doi: [10.1088/0004-6256/140/2/462](https://doi.org/10.1088/0004-6256/140/2/462)

Astropy Collaboration, Robitaille, T. P., Tollerud, E. J., et al. 2013, A&A, 558, A33, doi: [10.1051/0004-6361/201322068](https://doi.org/10.1051/0004-6361/201322068)

Barnes, P. J., Muller, E., Indermuhle, B., et al. 2015, ApJ, 812, 6, doi: [10.1088/0004-637X/812/1/6](https://doi.org/10.1088/0004-637X/812/1/6)

Beerer, I. M., Koenig, X. P., Hora, J. L., et al. 2010, ApJ, 720, 679, doi: [10.1088/0004-637X/720/1/679](https://doi.org/10.1088/0004-637X/720/1/679)

Benjamin, R. A., Churchwell, E., Babler, B. L., et al. 2003, PASP, 115, 953, doi: [10.1086/376696](https://doi.org/10.1086/376696)

Beuther, H., Walsh, A., Wang, Y., et al. 2019, A&A, 628, A90, doi: [10.1051/0004-6361/201935936](https://doi.org/10.1051/0004-6361/201935936)

Bitran, M., Alvarez, H., Bronfman, L., May, J., & Thaddeus, P. 1997, A&AS, 125, 99, doi: [10.1051/aas:1997214](https://doi.org/10.1051/aas:1997214)

Bronfman, L., Alvarez, H., Cohen, R. S., & Thaddeus, P. 1989, ApJS, 71, 481, doi: [10.1086/191384](https://doi.org/10.1086/191384)

Brunt, C. M., Kerton, C. R., & Pomerleau, C. 2003, ApJS, 144, 47, doi: [10.1086/344245](https://doi.org/10.1086/344245)

Canfield, P. C. 2020, Reports on Progress in Physics, 83, 016501, doi: [10.1088/1361-6633/ab514b](https://doi.org/10.1088/1361-6633/ab514b)

- Carey, S., Ali, B., Berriman, B., et al. 2008, *Spitzer Mapping of the Outer Galaxy (SMOG)*, Spitzer Proposal ID 50398
- Carey, S. J., Noriega-Crespo, A., Mizuno, D. R., et al. 2009, *PASP*, 121, 76, doi: [10.1086/596581](https://doi.org/10.1086/596581)
- Churchwell, E., Babler, B. L., Meade, M. R., et al. 2009, *PASP*, 121, 213, doi: [10.1086/597811](https://doi.org/10.1086/597811)
- Contreras, Y., Schuller, F., Urquhart, J. S., et al. 2013, *A&A*, 549, A45, doi: [10.1051/0004-6361/201220155](https://doi.org/10.1051/0004-6361/201220155)
- Csengeri, T., Urquhart, J. S., Schuller, F., et al. 2014a, *A&A*, 565, A75, doi: [10.1051/0004-6361/201322434](https://doi.org/10.1051/0004-6361/201322434)
- . 2014b, *A&A*, 565, A75, doi: [10.1051/0004-6361/201322434](https://doi.org/10.1051/0004-6361/201322434)
- Cygnus-X Team. 2020, *Cygnus-X: A Spitzer Legacy Survey of the Cygnus-X Complex*, IPAC, doi: [10.26131/IRSA402](https://doi.org/10.26131/IRSA402)
- Dame, T. M., Hartmann, D., & Thaddeus, P. 2001, *ApJ*, 547, 792, doi: [10.1086/318388](https://doi.org/10.1086/318388)
- Dame, T. M., Ungerechts, H., Cohen, R. S., et al. 1987, *ApJ*, 322, 706, doi: [10.1086/165766](https://doi.org/10.1086/165766)
- Dawson, J. R., Jones, P. A., Purcell, C., et al. 2022, *MNRAS*, 512, 3345, doi: [10.1093/mnras/stac636](https://doi.org/10.1093/mnras/stac636)
- Elia, D., Molinari, S., Schisano, E., et al. 2017, *MNRAS*, 471, 100, doi: [10.1093/mnras/stx1357](https://doi.org/10.1093/mnras/stx1357)
- Elia, D., Merello, M., Molinari, S., et al. 2021, *MNRAS*, 504, 2742, doi: [10.1093/mnras/stab1038](https://doi.org/10.1093/mnras/stab1038)
- Ellsworth-Bowers, T. P., Rosolowsky, E., Glenn, J., et al. 2015, *ApJ*, 799, 29, doi: [10.1088/0004-637X/799/1/29](https://doi.org/10.1088/0004-637X/799/1/29)
- GLIMPSE team. 2020, *Galactic Legacy Infrared Midplane Survey Extraordinaire (GLIMPSE)*, IPAC, doi: [10.26131/IRSA405](https://doi.org/10.26131/IRSA405)
- Grabelsky, D. A., Cohen, R. S., Bronfman, L., Thaddeus, P., & May, J. 1987, *ApJ*, 315, 122, doi: [10.1086/165118](https://doi.org/10.1086/165118)
- Harris, C. R., Millman, K. J., van der Walt, S. J., et al. 2020, *Nature*, 585, 357, doi: [10.1038/s41586-020-2649-2](https://doi.org/10.1038/s41586-020-2649-2)
- Heyer, M. H., Brunt, C., Snell, R. L., et al. 1998, *ApJS*, 115, 241, doi: [10.1086/313086](https://doi.org/10.1086/313086)
- Hora, J., Bontemps, S., Megeath, T., et al. 2007, *A Spitzer Legacy Survey of the Cygnus-X Complex*, Spitzer Proposal ID #40184
- Hunter, J. D. 2007, *Computing in Science and Engineering*, 9, 90, doi: [10.1109/MCSE.2007.55](https://doi.org/10.1109/MCSE.2007.55)
- Irabor, T., Hoare, M. G., Burton, M., et al. 2023, *MNRAS*, 520, 1073, doi: [10.1093/mnras/stad005](https://doi.org/10.1093/mnras/stad005)
- Jackson, J. M., Rathborne, J. M., Shah, R. Y., et al. 2006, *ApJS*, 163, 145, doi: [10.1086/500091](https://doi.org/10.1086/500091)
- Jayasinghe, T., Dixon, D., Povich, M. S., et al. 2019, *MNRAS*, 488, 1141, doi: [10.1093/mnras/stz1738](https://doi.org/10.1093/mnras/stz1738)
- Kerton, C. R., Wolf-Chase, G., Arvidsson, K., Lintott, C. J., & Simpson, R. J. 2015, *ApJ*, 799, 153, doi: [10.1088/0004-637X/799/2/153](https://doi.org/10.1088/0004-637X/799/2/153)
- Krumholz, M. R., & McKee, C. F. 2020, *MNRAS*, 494, 624, doi: [10.1093/mnras/staa659](https://doi.org/10.1093/mnras/staa659)
- Leung, H. O., & Thaddeus, P. 1992, *ApJS*, 81, 267, doi: [10.1086/191693](https://doi.org/10.1086/191693)
- Lumsden, S. L., Hoare, M. G., Urquhart, J. S., et al. 2013, *ApJS*, 208, 11, doi: [10.1088/0067-0049/208/1/11](https://doi.org/10.1088/0067-0049/208/1/11)
- McKinney, W. 2010, in *Proceedings of the 9th Python in Science Conference*, Vol. 445, Austin, TX, 51–56
- McKinney, W. 2011, *Python for High Performance and Scientific Computing*, 14
- Mège, P., Russeil, D., Zavagno, A., et al. 2021, *A&A*, 646, A74, doi: [10.1051/0004-6361/202038956](https://doi.org/10.1051/0004-6361/202038956)
- MIPSGAL team. 2020, *A 24 and 70 Micron Survey of the Inner Galactic Disk with MIPS (MIPSGAL)*, IPAC, doi: [10.26131/IRSA435](https://doi.org/10.26131/IRSA435)
- Molinari, S., Pezzuto, S., Cesaroni, R., et al. 2008, *A&A*, 481, 345, doi: [10.1051/0004-6361:20078661](https://doi.org/10.1051/0004-6361:20078661)
- Molinari, S., Baldeschi, A., Robitaille, T. P., et al. 2019, *MNRAS*, 486, 4508, doi: [10.1093/mnras/stz900](https://doi.org/10.1093/mnras/stz900)
- Motte, F., Bontemps, S., & Louvet, F. 2018, *ARA&A*, 56, 41, doi: [10.1146/annurev-astro-091916-055235](https://doi.org/10.1146/annurev-astro-091916-055235)
- NASA/IPAC Infrared Science Archive. 2020, *WISE All-Sky 4-band Atlas Coadded Images*, IPAC, doi: [10.26131/IRSA151](https://doi.org/10.26131/IRSA151)
- Ochsenbein, F., Bauer, P., & Marcout, J. 2000, *A&AS*, 143, 23, doi: [10.1051/aas:2000169](https://doi.org/10.1051/aas:2000169)
- PHPDP team. 2020, *Herschel PACS Highly Processed Data Products (PHPDP)*, IPAC, doi: [10.26131/IRSA82](https://doi.org/10.26131/IRSA82)
- Price-Whelan, A. M., Sipőcz, B. M., Günther, H. M., et al. 2018, *AJ*, 156, 123, doi: [10.3847/1538-3881/aabc4f](https://doi.org/10.3847/1538-3881/aabc4f)
- Purcell, C. R., Hoare, M. G., Cotton, W. D., et al. 2013, *ApJS*, 205, 1, doi: [10.1088/0067-0049/205/1/1](https://doi.org/10.1088/0067-0049/205/1/1)
- Reid, M. J., Menten, K. M., Brunthaler, A., et al. 2019, *ApJ*, 885, 131, doi: [10.3847/1538-4357/ab4a11](https://doi.org/10.3847/1538-4357/ab4a11)
- Schuller, F., Urquhart, J. S., Csengeri, T., et al. 2021, *MNRAS*, 500, 3064, doi: [10.1093/mnras/staa2369](https://doi.org/10.1093/mnras/staa2369)
- Simpson, R. J., Povich, M. S., Kendrew, S., et al. 2012, *MNRAS*, 424, 2442, doi: [10.1111/j.1365-2966.2012.20770.x](https://doi.org/10.1111/j.1365-2966.2012.20770.x)
- Taylor, A. R., Gibson, S. J., Peracaula, M., et al. 2003, *AJ*, 125, 3145, doi: [10.1086/375301](https://doi.org/10.1086/375301)
- Taylor, M. B. 2005, in *Astronomical Society of the Pacific Conference Series*, Vol. 347, *Astronomical Data Analysis Software and Systems XIV*, ed. P. Shopbell, M. Britton, & R. Ebert, 29
- Urquhart, J. S., König, C., Giannetti, A., et al. 2018, *MNRAS*, 473, 1059, doi: [10.1093/mnras/stx2258](https://doi.org/10.1093/mnras/stx2258)
- Virtanen, P., Gommers, R., Oliphant, T. E., et al. 2020, *Nature Methods*, 17, 261, doi: <https://doi.org/10.1038/s41592-019-0686-2>

Walsh, A. J., Lo, N., Burton, M. G., et al. 2008, PASA, 25, 105, doi: [10.1071/AS07053](https://doi.org/10.1071/AS07053)

Wolf-Chase, G., Kerton, C. R., Devine, K., et al. 2021, ApJ, 911, 28, doi: [10.3847/1538-4357/abe87a](https://doi.org/10.3847/1538-4357/abe87a)

Wright, E. L., Eisenhardt, P. R. M., Mainzer, A. K., et al. 2010, AJ, 140, 1868, doi: [10.1088/0004-6256/140/6/1868](https://doi.org/10.1088/0004-6256/140/6/1868)